

# Electronic, Optical, and Elastic Properties of CaFI Monolayer and Acoustic Phonon Dispersion at Hypersonic Frequencies Using Density Functional Theory and beyond with Random Phase Approximation and Bethe–Salpeter Equation

Mohamed Barhoumi\* and Nouredine Sfina

Cite This: *ACS Omega* 2022, 7, 15338–15349

Read Online

ACCESS |



Metrics &amp; More

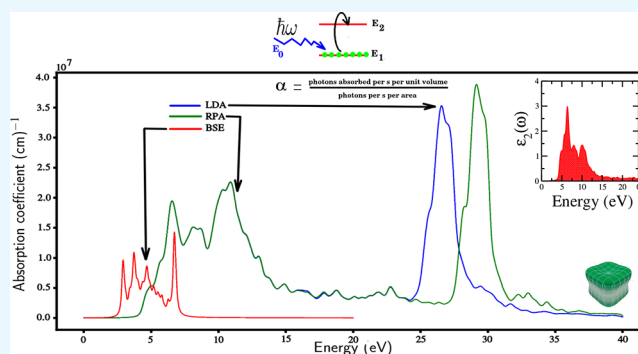


Article Recommendations



Supporting Information

**ABSTRACT:** The extraordinary properties of graphene have motivated us to investigate a novel 2D compound. In this framework, we study the structural, vibrational, electronic, optical, and elastic properties of a new two-dimensional CaFI monolayer, using DFT, GW, RPA, and BSE methodologies. The phonon dispersion curve of the CaFI monolayer exhibited no unstable phonon modes, confirming that this 2D sheet is dynamically stable. Our GW calculations show that the indirect bandgap energy value of CaFI is 6.52 eV. Interestingly, the bandgap rapidly decreased by improving the electric field value. Our BSE computations indicate that this monolayer becomes translucent when the incident light frequency exceeds the plasma frequency (6.50 eV). Also, we have computed the second and third elastic constants of CaFI by combining the DFT and RPA approaches with the homogeneous deformation method. Additionally, the longitudinal acoustic phonon dispersion of CaFI was studied. We have determined that the longitudinal acoustic wave velocity in our sheet is higher than the LA wave velocity of germanium measured using Brillouin or ultrasonic techniques.



## INTRODUCTION

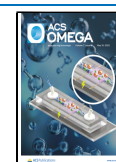
Graphene<sup>1–3</sup> is a two-dimensional crystal of carbon atoms spread evenly in a hexagonal honeycomb-shaped lattice. In nature, the stacking of layers of graphene forms graphite, which is commonly found in our pencil mines. Graphene is a miracle material<sup>4,5</sup> that humankind stumbled upon almost by accident, in experiments that saw rolls of tape and flying frogs scroll by. Graphene is impermeable to molecules and exhibits high thermal and electrical conductivity,<sup>6,7</sup> permitting electrons to flow much faster than silicon. It is also a transparent conductor, exceptionally combining optical and electrical functionality. Graphene allows a wide variety of potential applications,<sup>8</sup> from electronics to composite materials,<sup>9</sup> and it is relatively inexpensive to produce compared with other materials. Although it is effective at quickly transporting electrons, graphene has a handicap: unlike the materials from which the transistors in our computers are created, it is not a semiconductor. This handicap opened the highway to identify unique two-dimensional materials (2D) by mechanical exfoliation<sup>10</sup> or physical vapor deposition.<sup>11</sup> Among these 2D compounds are silicene,<sup>12</sup> transition metal dichalcogenides (TMDs),<sup>13</sup> phosphorene,<sup>14,15</sup> Janus transition metal dichalcogenides (JTMDs),<sup>16</sup> transition-metal compounds (TMC),<sup>17,18</sup> and so on.<sup>19–22</sup> Unfortunately, the TMD band gap energy ( $E_g$ )

value does not exceed 3.0 eV; consequently, they are not fitting for optoelectronic applications, for example, in photocatalytic water splitting.<sup>23,24</sup> Accordingly, the quest for new 2D materials with wide band gaps and stable dynamically became required to circumvent this lack. The field of investigation on two-dimensional materials has been very effective for developing new composites<sup>25,26</sup> that have distinct features compared with other elements, which can be employed in the production of new electronic devices. In this direction, we have recently achieved, a new type of systems of films, which is 2D halides.<sup>26,27</sup> Theoretically, there are several investigations on the physical properties of halides. For instance, the electronic features of Pb–I insufficient lead halide perovskites have been calculated by Zheng et al.<sup>28</sup> From ab initio calculations, Barhoumi et al.<sup>29</sup> have estimated the electronic and optical aspects of bismuth oxyhalides. Furthermore, using density functional theory (DFT)<sup>30</sup> and beyond,<sup>27</sup> the electro-optic

Received: November 15, 2021

Accepted: April 15, 2022

Published: April 26, 2022



properties of PbFCl and PbFI monolayers have been discovered. The structural and electronic properties of the CaFI bulk have been explored by El Haj Hassan and colleagues.<sup>31</sup> The structural stabilities and electronic structure of high-angle grain borders in crystalline cesium lead halides were explored by Guo et al.<sup>32</sup> Structural, elastic, electronic, and optical properties of lithium halides (LiF, LiCl, LiBr, and LiI) have fully been determined using the first-principle calculations.<sup>33</sup> Experimentally, Tombe and his colleagues<sup>34</sup> have investigated the dielectric properties of heterogeneous halide (X = I, Cl, Br) methylammonium. The architectural and electronic properties of multifunctional composite materials of organometal halide perovskites were investigated by Klejna.<sup>35</sup> Senol and Erdem<sup>36</sup> have investigated the hydrothermal synthesis of Li codoped Zn<sub>0.98</sub>Mg<sub>0.02</sub>O nanoparticles and their structural, optical, and electrical properties. The three tin oxide halides, Sn<sub>7</sub>O<sub>4</sub>Cl<sub>6</sub>, Sn<sub>7</sub>O<sub>4</sub>Br<sub>6</sub>, and Sn<sub>4</sub>OI<sub>6</sub>, were synthesized by solid-state reactions of SnO and SnX<sub>2</sub> (X = Cl, Br, I).<sup>37</sup> Giordano et al.<sup>38</sup> have shown that n-doping of mesoporous TiO<sub>2</sub> is accomplished by facile post-treatment of the films with lithium salts. Although there has been a massive amount of work on the electronic and optical characteristics of halides, no experimental or theoretical research on the electronic, optical, and elastic properties of a CaFI monolayer and acoustic phonon dispersion at hypersonic frequencies in CaFI has been done yet. In this paper, for the first time, we apply density functional theory and beyond to examine the structural, vibrational, electronic, optical, and elastic aspects of CaFI. The actual work is divided into different sections: after this introduction, the next section contains the computational methods, which is followed by our results and, lastly, our conclusions.

## COMPUTATIONAL DETAILS

We have used the Vienna ab initio simulation package (VASP)<sup>39</sup> code to make accurate predictions applying density functional theory. Interactions between electrons are addressed within the projector-augmented wave (PAW).<sup>40</sup> Either Ceperly and Alder's (CA) local density approximation (LDA)<sup>41</sup> and Perdew–Burke–Ernzerhof's (PBE) generalized gradient approximation (GGA)<sup>42</sup> with a plane wave cutoff of 500 eV (with 0.2 eV broaden for the optical calculations) and a 12 × 12 × 1 k-point mesh were employed to simulate exchange and correlation. For the hybrid Heyd–Scuseria–Ernzerhof (HSE)<sup>43</sup> predictions, we have applied the same parameters. We have employed the adiabatic-connection fluctuation–dissipation theorem (ACFDT) in random phase approximation (RPA)<sup>44</sup> with a cutoff of 700 eV and Brillouin-Zone (BZ) sample with 12 × 12 × 1. All RPA estimations were achieved employing the PBE orbitals and PBE one-electron energies (RPA@PBE). As mentioned before in ref 45, we have performed the G<sub>0</sub>W<sub>0</sub> type with a GW cutoff of 700 eV and 208 bands, which produces precise band gap energy data (see SI). It should be noted that for a better precise band gap value, we have employed an energy cutoff of 700 eV and a GW cutoff of 700 eV. Because when a slight cutoff energy is employed, there is a false-convergence behavior of the band gap.<sup>45</sup> Our GW computations are of the G<sub>0</sub>W<sub>0</sub> kind no self-consistency is included. The Bethe–Salpeter equation (BSE)<sup>46</sup> was used to express the absorption spectra of our monolayer. To stop important interactions between the periodically reproduced pictures, enough spacing between the layers (more than 17 Å) was applied. With residual forces less than 0.0001 eV/Å, the

CaFI monolayer was completely relaxed. The density functional perturbation theory (DFPT)<sup>47</sup> with a 5 × 5 × 1 supercell was used to establish the dynamical stability of this layer. To quantify the correlation-exchange energy in HSE, the correlation-exchange  $E_{xc}$  expression was first constructed in PBE and then again in PBE0:

$$E_{xc}^{PBE} = E_x^{PBE} + E_c^{PBE} \quad (1)$$

$$E_{xc}^{PBE0} = \alpha \times E_x^{HF} + (1 - \alpha) \times E_x^{PBE} + E_c^{PBE} \quad (2)$$

In the Hartree–Fock (HF) approach, the nonlocal Fock (exact) exchange energy is not a density functional. This exchange exactly removes the deceptive self-interaction, however, and needs no description of electronic correlation. The exchange itself is pretty long-ranged (LR), declining unique as  $\frac{1}{r}$ .

$$\frac{1}{r} = SR + LR = \frac{\text{erfc}(\omega r)}{r} + \frac{\text{erf}(\omega r)}{r} \quad (3)$$

A hybrid HSE (XC) functional is a combination of the HF and GGA approaches, driven by the observation that the HF approximation overvalues the significant gap while the LDA or GGA estimations undervalue it.

$$E_{xc}^{HSE} = \alpha \times E_x^{HF,SR}(\omega) + (1 - \alpha) \times E_x^{PBE,SR}(\omega) + E_x^{PBE,LR}(\omega) + E_c^{PBE} \quad (4)$$

The HSE group has a long- and short-ranged (SR) participation partitioning, as well as screening within the HF term itself. The HSE03 hybrid functional, for example, is described by this way:

$$E_{xc}^{HSE03} = \frac{1}{4}E_x^{sr,\mu} + \frac{3}{4}E_x^{PBE,sr,\mu} + E_x^{PBE,lr,\mu} + E_c^{PBE} \quad (5)$$

Where

$$E_x^{sr,\mu} = -\frac{e^2}{2} \sum_{kn,qm} 2w_k f_{kn} 2w_q f_{qm} \times \iint d^3r d^3r' \frac{\text{erfc}(\mu|r - r'|)}{|r - r'|} \times \phi_{kn}^*(r) \phi_{qm}(r) \phi_{qm}^*(r') \phi_{kn}(r') \quad (6)$$

It is worth noting that just the exchange portion of the electron–electron connection is divided into a short (sr) and long-range (lr) portion. The ranging separation associated with a specific distance (2/μ) during which short-range interactions become minimal is defined by the quantity μ.  $\phi_{kn}(r)$  are Bloch states, and  $f_{kn}$  are occupational numbers (for more details, see ref 48). The application of the HSE functional to substances with varying degrees of localization results in frequent errors. Because the Hartree–Fock exchange is heavily converged around the supercell size, HSE may predict an inaccurate ground state for the negatively charged. As a result, we used the RPA methodology. The energy of exchange–correlation is developed as having:

$$E_{xc}^{RPA} = E_x^{EX} + E_{RPA}^c \quad (7)$$

$E_x^{EX}$  is exchange-exact energy and  $E_{RPA}^c$  is the correlation term RPA. Where the  $E_x^{EX}$  energy is written in the following form:

$$E_x^{EX} = -\sum_{ij} f_i f_j \iint \psi_i^*(r) \psi_j(r) v(r, r') \times \psi_j^*(r') \psi_i(r') dr dr' \quad (8)$$

The RPA applied to cyclic infinite systems is a good way to resolve their polarizabilities per unit cell and talk about their excitation spectra. On the basis of the higher-order modes of the polarization propagator, the irresponsibility of electron correlation effects of this HF technique can still be alleviated in future designs. Long-range van der Waals (vdW) interactions are easily incorporated into the RPA correlation energy. Also, the  $E_c^{RPA}$  energy is written in the following form:

$$E_c^{RPA} = \frac{1}{2\pi} \int_0^\infty d\omega \text{Tr}[\ln(1 - \chi^0(i\omega)v) + \chi^0(i\omega)v] \quad (9)$$

$\chi^0(r, r', i\omega)$ , is the Kohn–Sham (KS) independent particle response function of the reference system  $\lambda = 0$  and is known explicitly in terms of orbitals  $\psi_i(r)$  with a single particle (KS), orbital energies  $\epsilon_i$  and occupancy factors  $f_{ij}$  (for more details see SI). Moreover, as compared with the DFT approach, the BSE program enhances the correlation term. The correlation energy is calculated using the following formula:

$$E_c^{BSE} = \frac{-1}{2\Omega_{BZ}} \sum_{G,S,S'} f_S n_{GS} n_{GS'}^* \nu_G \left[ \delta_{SS'} \theta(E_S) - \int_0^1 d\lambda \sum_{\alpha\alpha'} A_{S\alpha}^\lambda [N_{\alpha\alpha'}]^{-1} A_{S\alpha'}^{\lambda*} \theta(\text{Re}E_\alpha^\lambda) \right] \quad (10)$$

The eigenvalues and eigenstates of the BSE Hamiltonian at coupling strength  $\lambda$  are  $E_\alpha^\lambda$  and  $A_\alpha^\lambda(S)$ . The excitation population is  $f_S$ , and the plane wave is  $n_{GS}$ .  $S$  symbolizes an electron–hole excitation. For more definitions of parameters, see ref 49. The optical qualities are calculated through using  $\epsilon(\omega)$  complex dielectric function, which is distinguished as

$$\epsilon(\omega) = \epsilon_1(\omega) + i\epsilon_2(\omega) \quad (11)$$

The momentum array parts between the full and empty electronic states provide the imaginary part  $\epsilon_2(\omega)$ . The dielectric function's real portion  $\epsilon_1(\omega)$  can be summarized as follows:

$$\epsilon_1(\omega) = 1 + \frac{2}{\pi} \mathcal{P} \int_0^\infty \frac{\omega' \epsilon_2(\omega')}{\omega'^2 - \omega^2} d\omega' \quad (12)$$

$\mathcal{P}$  specifies the Cauchy high emphasis of the integral, ignoring the propensity's input to the integral at  $\omega = \omega'$ . We have used dipole approximation to compute absorption spectra, which means that the moment change from the initial state to the end state is ignored. The dielectric function is determined using the present description, which compares the full and empty states of the dipole array  $P$ . Using the continuity equation, we estimated the absorption coefficient ( $\alpha(\omega)$ ) from the dielectric function:

$$\alpha(\omega) = \sqrt{2} \omega [\sqrt{\epsilon_1^2(\omega) + \epsilon_2^2(\omega)} - \epsilon_1(\omega)]^{1/2} \quad (13)$$

## RESULTS AND DISCUSSION

In Figure 1, we have offered the side view of the CaFI thin film. Our CaFI crystal system is tetragonal,  $a = b \neq c$  and  $\alpha = \beta = \gamma = 90^\circ$ , as mentioned in SI. The lengths of the Ca–I and Ca–F bonds are 3.30 and 4.68 Å (HSE), accordingly. When the hybrid HSE functional is applied, the F–Ca–I and F–Ca–F bond angles are 49.70 and 73.22°, respectively. We have also established that with LDA the lattice constants  $a$ , which is around 3.85 Å, whereas with GGA, it is about 3.94 Å.

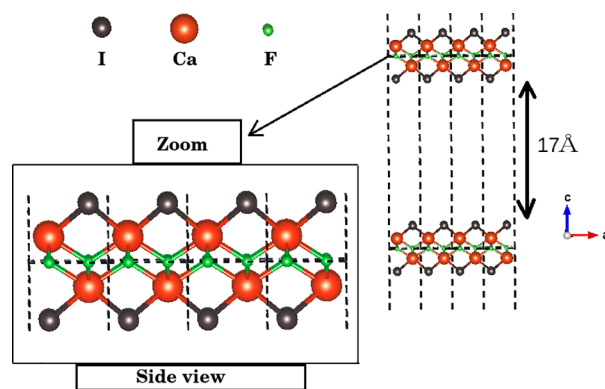


Figure 1. Side view of the crystal structure of CaFI monolayer.

However, the hybrid HSE calculations outperform the LDA and GGA findings, with the lattice constant being  $\sim 3.91$  Å. It is worth noting that the CaFI sheet is 6.70 Å (HSE) thick. As previously stated, applying the hybrid HSE functional to compounds with varying degrees of localization results in systematic errors: due to the high convergence of the Hartree–Fock exchange in the supercell dimension. HSE may infer an inaccurate ground state for negatively charged compounds. As a result, we have employed the RPA approach to better represent the architectural structure of our sheet. We have provided our RPA results in Table 1, along with DFT

Table 1. Bond Lengths (Å), Bond Angles (deg), and Lattice Constant (Å) of the CaFI Monolayer, Using Different Approaches

	Ca–I	Ca–F	F–Ca–I	F–Ca–F	$a$ (Å)	$c/a$
LDA	3.28	4.59	49.68	73.20	3.85	4.41
GGA	3.29	4.64	49.69	73.21	3.94	4.31
HSE	3.30	4.68	49.70	73.22	3.91	4.34
RPA	3.30	4.67	49.69	73.21	3.90	4.35

calculations of the CaFI monolayer bond lengths and lattice constants. A noticeable point is that we put more details regarding the CaFI geometry structure like symmetry, point group, or space group in SI. Since it explicitly incorporates a fraction of the electron correlation energy to make considerable physical effects without increasing the computing expense, the RPA approach accurately reflects the shape. The RPA algorithm can solve more efficiently for intermolecular interaction energies than the normal DFT technique with empirical dispersion corrections. Then, using the DFPT-PBE method, we have estimated the phonon spectra of our layer. In Figure 2, the phonon dispersion curves are sketched along the path  $\Gamma$ -X-M- $\Gamma$ . The law of vibrational characteristics states the following: if there are no fictitious frequencies in the spectra, the monolayer is dynamically stable; anything other than that, it is not dynamically stable. CaFI is dynamically stable in this direction, as no imaginary frequency appears in its spectra. There is a weakly unstable phonon branch near to the Brillouin zone center: this is not a real physical impact but reflects the well-known difficulty in performing numerical convergence for the flexural phonon mode for 2D materials, which was discussed in previous works of Fal'ko et al.<sup>50,51</sup> The electronic properties of the sheet addressed here, such as partial density of states (PDOS) and total density of states (TDOS), were explored. In this way, PDOS and TDOS are depicted together

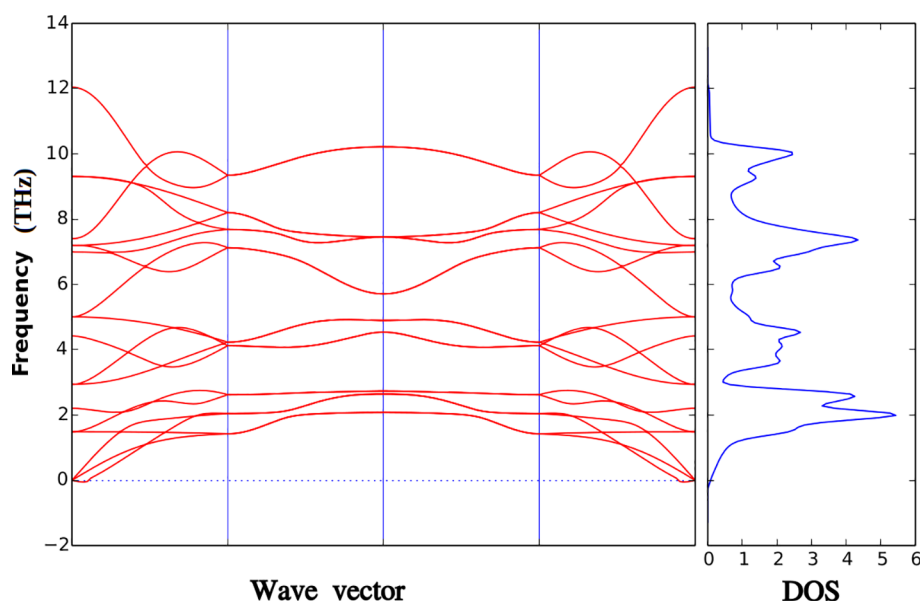


**Figure 2.** Phonon dispersion curves of the CaFI sheet.

in Figure 3, respectively, using LDA, GGA, and HSE functionals. All approaches reveal that the I atom's orbitals

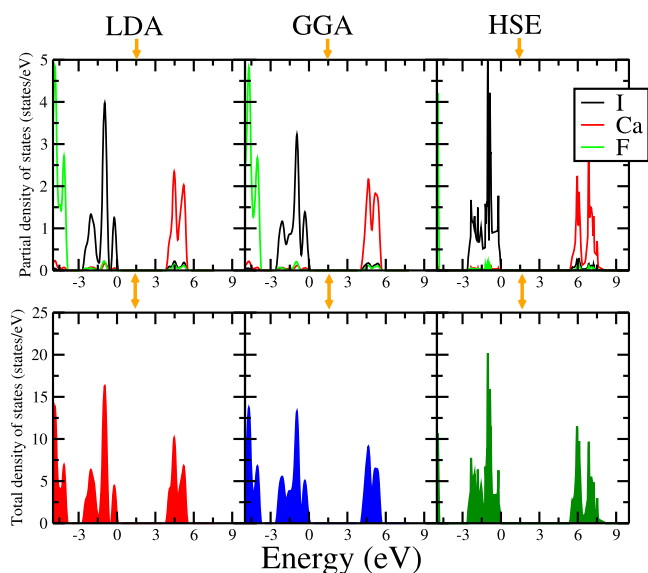


**Figure 3.** Partial density of states and total density of states of CaFI using LDA, GGA, and HSE, respectively.

create the top of the valence band, while the Ca atom donates to the bottom of the conduction band. We can also derive the band gap energy of this layer from the TDOS. Our LDA band gap energy result of CaFI is around 3.92 eV, while it is  $\sim 4.20$  eV when GGA-PBE is applied. Generally, when compared with experimental data,<sup>52</sup> LDA and GGA underestimated the band gap value. Therefore, we have rehearsed the HSE approach to minimize getting this wrong. Absolutely, the hybrid HSE functional is a combination of the HF and LDA (or GGA) approaches, motivated by the observation that HF overestimates the required band gap while LDA and GGA underestimate it. This hybrid functional generates a choice that is halfway between HF and DFT, resulting in a more realistic gap. Furthermore, it has long been recognized that the

local density approximation and the generalized gradient approximation do not reliably capture band gaps and that one must look beyond these methodologies to express these features. With the hybrid HSE functional, we have shown that the band gap value is around 5.50 eV in this context. Additionally, we have performed GGA and GW to support the findings obtained from the TDOS regarding the band gap value of CaFI with the band structure, which is illustrated in Figure 4. With the GGA-PBE band structures, we have

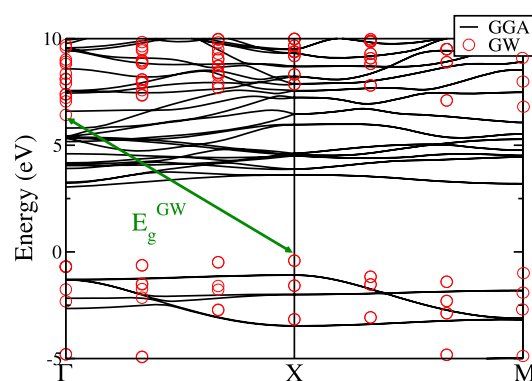


**Figure 4.** Band structures of CaFI with GGA and GW. 0 eV is selected as the Fermi level. An arrow denotes the band gap indirect  $E_g$ , while vertical lines denote the locations of high-symmetry sites.

acquired a band gap value of 4.20 eV, as depicted in TDOS-GGA. Nevertheless, as previously noted, the GGA band gap is not consistently anticipated. Significantly, we have gone beyond the hybrid HSE functional; indeed, we have rectified the band gap value inaccuracy using the GW approach. Definitely, in extended systems, the most widely used approximation is the GW model; in the case of HF, the bare Coulomb contact in the exchange term is replaced by a dynamically screened interaction.<sup>53</sup> This reduces the far too large HF eigenvalue gap in solids and brings it closer to experiment in generality. The band gaps of semiconductors and insulators<sup>54</sup> are usually well represented by GW. GW has previously produced electron addition and elimination energies

through extensive experimentation. These accomplishments place GW near the top of any list of first-principles electronic structure techniques in terms of computational value, or exactness for computational cost. Because of GW adaptability, present occupations in physics, chemistry, and materials science will continue to grow in the future. The density and one-body density array are fundamentally generalized by GW. In this direction, as seen in Figure 4, the GW approximation guides vital modifications: the indirect band gap value at the  $\Gamma$ -X-points grows from 4.20 eV (DFT) to 6.52 eV (GW), which is larger than the band gap of PbFCl (6.38 eV with GW), ScOI, and InOF (4.0 eV with HSE) 2D monolayers.<sup>26</sup> Too, GW changes detected at the other high symmetry points, for instance, at X the lowest energy transition improves from 3.55 eV (GGA) to 8.12 eV with GW. Note that both the conduction band minimum (CBM) and valence band maximum (VBM) are located at the  $\Gamma$  and X-point, accordingly. In general, the dipole correction has a considerable impact on the electrostatic potential propagation perpendicular to the CaFI sheet.<sup>55</sup> Our sheet electrostatic potential with dipole correction is shown in Figure 5. The work

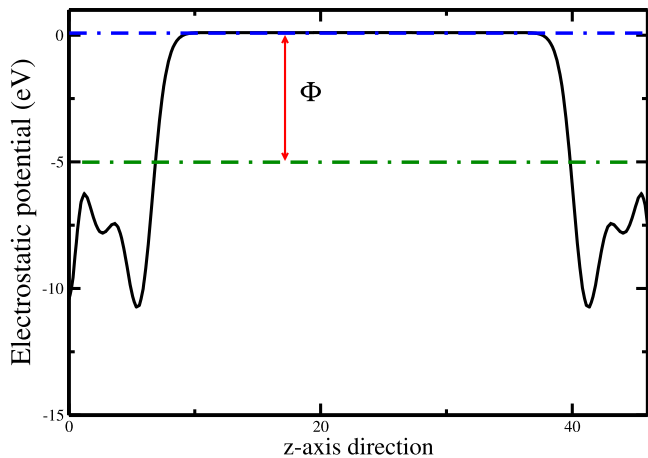


**Figure 5.** CaFI monolayer electrostatic potential. The vacuum and Fermi level were used to calculate the work function. The top and bottom vacuum levels (VCL) are indicated by dashed green lines. The Fermi level is represented by the dashed blue line.

function  $\Phi$  has been established in this framework. The minimum energy required for an electron to transit between the Fermi and vacuum levels is  $\Phi$ . Also,  $\Phi$  refers to the capacity of an electron to leave the compound's surface. In our case, the difference in work function is almost ignored with  $\Phi_{Ca} = \Phi_F = \Phi_I = \Phi = 4.98$  eV, which is larger than the functional work of the  $\text{In}_2\text{TeO}$  monolayer ( $\Phi = 4.16$  eV).<sup>56</sup> The influence of the electric field on the band gap in two sheets was recently examined.<sup>57</sup> For example, Zheng et al.<sup>58</sup> have reported that applying electric fields in distinct angles reduced or improved the equivalent field in zigzag BN nanoribbons, leading to decreased or increased band gap due to the Stark effect. As a result of the Stark impact, Liu et al.<sup>59</sup> have reported that  $\text{MoS}_2$  exhibited varied band gap modifications for various types of  $\text{MoS}_2$  bilayer. As previously done for graphene,<sup>60</sup> we have assessed the effects of the electric field  $E$  on the band structures of the monolayer, as shown in Figure 6. By using the GGA-PBE model, we have applied an external electric field to the CaFI layer in the  $z$ -direction, with a range of 0.0, 0.5, and 1.0 V/Å. The CaFI band gap energy

and band locations are readily tweaked, according to our findings. A little vertical electric field has been obtained, which reduces the band gap value. For instance, a 0.5 V/Å increase in electric field intensity can reduce the band gap from 4.20 to 0.1 eV while preserving the indirect gap type. As a result, we can make a semiconductor to metal transition with a field strength of more than 0.5 V/Å. The interaction of an electron with a photon is done, like any interaction, with the protection of energy and the wave vector. The wave vector of the photon being much lower than that of the electrons, the direct optical transitions between the valence band and the conduction appear vertical in the electron band diagram. In the case of a band gap semiconductor indirect, optical transitions through the gap can only take place through an additional interaction, for example, that of a phonon. Absorption, transmission, reflection, dispersion, and emission are all examples of how light reacts with a matter in solid-state physics. The investigation of solid optical characteristics has been shown to be a valuable strategy in gaining a better knowledge of material electronic structure. As a consequence, semiconductor optical properties have provided useful insight into several aspects of their physical parameters, such as their electronic and vibrational modes. Some optical processes have given data about the geometry of semiconductors heterostructures. The optical properties of 2D are important for a variety of applications, including fibreoptic coatings and lens coverings. The weathering resistance of 2D is primarily dependent on its optical qualities, particularly when ultraviolet absorption is involved. In general, these properties reflect how elements react to the electromagnetic spectrum. The received radiation is partially transmitted, partly reflected, and partly absorbed by each object. Transmissivity, reflectivity, and absorptivity are optical qualities that describe a material's response to incoming radiation. Also, understanding optical qualities is useful in a variety of commercial and scientific jobs, such as planning, photonic devices, and so on. In this way, we have involved LDA, RPA, and BSE to predict the optical properties of the CaFI thin film, such as dielectric function, absorptivity, and index of refraction. Notably, all of the calculations shown here are for a polarization vector perpendicular to the  $c$ -axis. In Figure 7, we have illustrated the  $\epsilon_1(\omega)$  and  $\epsilon_2(\omega)$  parts, accordingly. In the  $\epsilon_1(\omega)$  spectra, we have found a greater peak around 4.56 eV with LDA and 4.57 eV with RPA. We have discovered that RPA produces results that are substantially identical to LDA. Even though RPA is one of the best nonperturbative approaches for determining the ground-state correlation energy of many-electron structures, it produced results that were close to LDA predictions. This is because RPA describes the short-ranged section of the correlation hole incorrectly. The electron–hole interaction can then be computed by adding vertex corrections' behind the RPA, which can be done in practice by resolving BSE. This results in high absorption and electron energy loss spectra in general. It is worth noting that the BSE formalism is unmistakably establishing itself as a new dynamic and accurate gadget in the arsenal of computational tools available to researchers for divining optical excitations in 2D systems. The GW-BSE approach's application to semiconducting 2D layers has explained and predicted several fascinating new physical features of these substances. It is important to note that in the baseline system, diagonalizing the BSE Hamiltonian appears to agree to help solve a linear eigenvalue complexity in the region of single excitations, whereas in its numerical

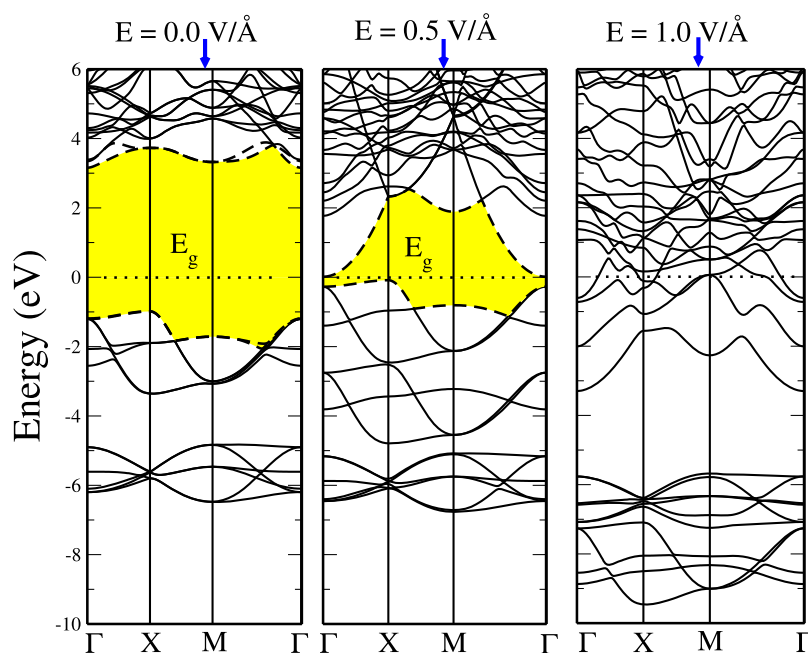


**Figure 6.** Using the GGA functional, the electronic band structures of CaFI monolayer as a function of applied electric field. The Fermi level is zeroed out.

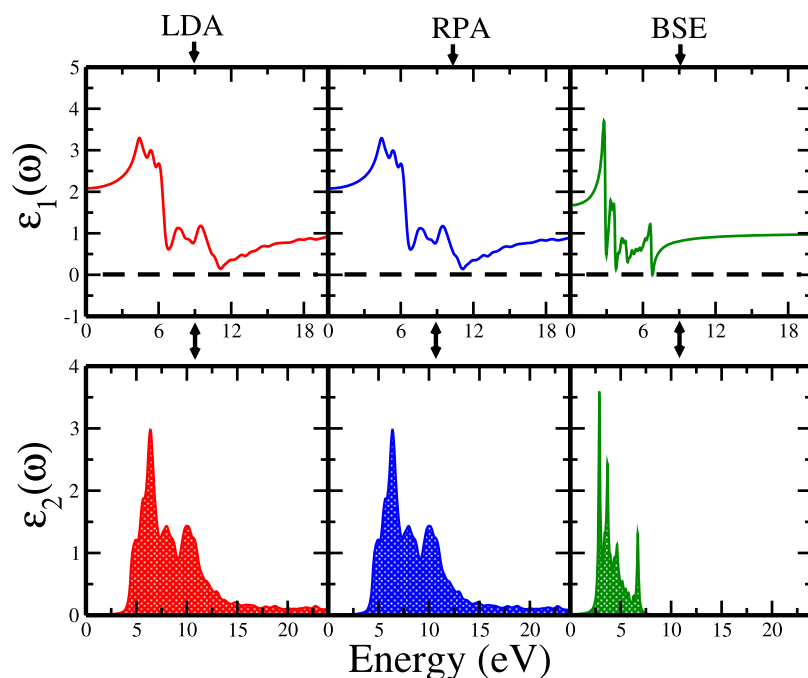


**Figure 7.** Imaginary part ( $\epsilon_2(\omega)$ ), and real part ( $\epsilon_1(\omega)$ ) of the dielectric function.

approach, it is nonlinear eigenvalue trouble that is much more difficult to establish from a computational perspective. Here, the optical transition between Ca *s*-states in the maximum valence band and I *p*-states in the minimum conduction band results in an impactful peak (maximum position) of 2.80 eV with BSE. LDA and RPA spectra have minimum energies of 11.1 and 11.2 eV, correspondingly. After using the BSE approach, the minimal CaFI spectrum is detected at an energy of 7.0 eV. If we look at the real portion of the dielectric function, we can observe that the fundamental element of the dielectric function does not pass through the 0 levels for this monolayer, when LDA and RPA are used. In addition, the

imaginary part  $\epsilon_2(\omega)$  of CaFI dielectric function, which is presented in Figure 7, validates this feat. If BSE is insinuated, we identify two notable peaks in the  $\epsilon_2(\omega)$  spectra of CaFI: 3.00 eV (6.5 eV with LDA and  $\sim 6.51$  eV with RPA) and 3.5 eV (10.40 eV with LDA and  $\sim 10.35$  eV with RPA). We have established that the transitions between Ca *s* and I *p*-states are represented by the peak at 3.00 eV. The crossovers between Ca *s* and F *p*-states are represented by another peak. We can analyze other optical parameters such as refractive index and reflectivity after generating the two portions of the dielectric function. In this context, we have calculated the CaFI monolayer absorption coefficient  $\alpha(\omega)$ , as can be seen in

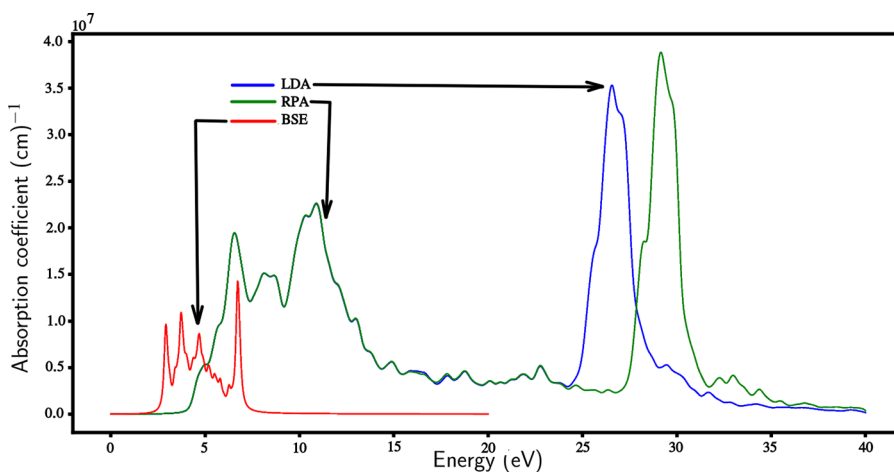


**Figure 8.** Absorption coefficient of CaFI monolayer, using LDA, RPA, and BSE, respectively.

**Figure 8.**  $\alpha$  is the distance that light of a particular frequency may penetrate an element before being absorbed. Radiation is just poorly absorbed in an element with a low absorption coefficient, and if the material is thin enough, it will appear transparent to that wavelength. The absorption coefficient is defined by the element as well as the wavelength of light absorbed. More exactly,  $\alpha$  displays the light's intensity degradation as it passes through a medium. For an optical approach, it can be defined as the sum of an element's absorption bridge per unit volume. Therefore, because spectra begin with a value difference of 0 eV, the absorption coefficient spectra of the CaFI show the semiconductor quality of this film. Herein, we have employed a wide range of energy from 0 to 40 eV. When BSE is employed, we see multiple peaks, one at 4.00 eV and the other at 6.50 eV. Moreover, with the BSE method, this layer has a good absorption coefficient in the 2.50–7.00 eV area. Consequently, we have revealed that when the frequency of the light source is greater than the resonance frequency (6.50 eV), the compound investigated here becomes translucent. Through using BSE methodology, we have investigated the reflectivity coefficient ( $n(\omega)$ ) and the reflectivity (%) of the CaFI monolayer in parallel with the absorptivity. In **Figure 9**, we display these parameters, namely the refractive index and the reflectance.  $n(\omega)$  is the amount of light that is rounded or refracted when it enters a monolayer. It is a physical quantity that can be used to differentiate a substance because it is a feature of a medium. For a given light wave, every transparent medium is defined by its refractive index. The following definition delivers the refractive index of every tiny layer dielectric:

$$n^2 = (n_r + in_i)^2 \quad (14)$$

$$n_r^2 - n_i^2 = 1 + \frac{Ne^2}{m\epsilon_0} \left[ \frac{\omega_0^2 - \omega^2}{(\omega_0^2 - \omega^2) + \omega^2\gamma^2} \right] \&2n_r \quad (15)$$

$$n = \frac{Ne^2}{m\epsilon_0} \left[ \frac{\omega r}{(\omega_0^2 - \omega^2) + \omega^2\gamma^2} \right] \quad (16)$$

The real part of the refractive index is  $n_r$  while the imaginary part is  $n_i$ . It has something to do with the weak layer absorption. The electrons' resonance frequency,  $\omega_0$ , varies from element to element.  $N$  is the number of atoms per unit volume,  $m$  is the electron's mass, and  $e$  is the electron's electric

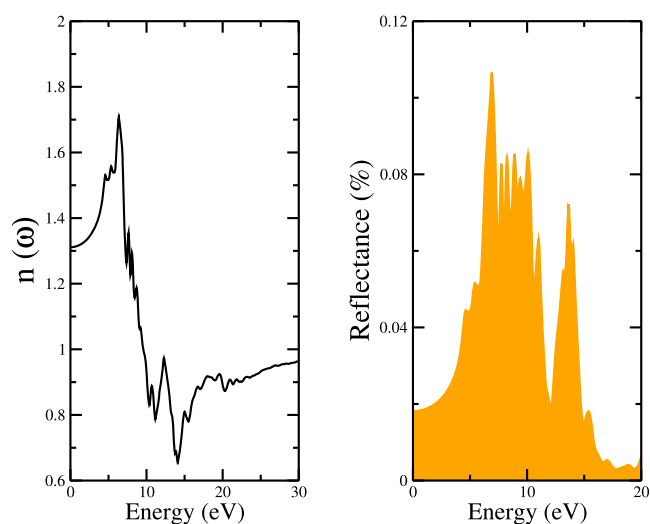


**Figure 9.** Reflectivity index ( $n(\omega)$ ) and the reflectance (%) of the CaFI monolayer, using the BSE approach.

current. The refractive index of our monolayer as a versus photon energy, from which we derive the static refractive index of this sheet, is  $\sim 1.31$  with BSE, as seen in **Figure 8**. We may also express another important statistic, the reflectance coefficient ( $R$ ), which represents the portion of energy exhibited at the solid's interface and can be calculated from the index of refraction:

$$R = \frac{(n - 1)^2 + K}{(n + 1)^2 + K} \quad (17)$$

where  $n$  is the refractive index,  $K$  is the extinction coefficient also called the attenuation index. The  $R$  reflectivity spectrum for this monolayer is displayed in **Figure 9**. We can see that  $R$  rises to around 0.107% (6.9 eV) and then starts to fall. The SOECs and TOECs of the CaFI monolayer were then calculated using DFT (LDA, GGA, and HSE) and RPA computations. The RPA procedure was chosen because it captures basic electron correlation influences such as midand long-range communications, as well as some static correlation even at the level of the bare Coulomb interaction kernel. These effects are largely lacking from the DFT explanation. As mentioned above, RPA outperforms the standard DFT (LDA, GGA, and HSE) technique in terms of intermolecular

**Table 2. CaFI Monolayer Second-Order Elastic Constants and Mechanical Characteristics in GPa**

	$C_{11}$	$C_{12}$	$C_{13}$	$C_{66}$	$C_{33}$	$C_{44}$	$G_{VRH}$	$\nu_{VRH}$	$E_{VRH}$	$B_{VRH}$
LDA	90.26	29.35	55.78	39.59	80.51	20.80	21.72	0.33	58.123	59.77
GGA	95.75	33.00	58.45	42.69	90.45	22.45	24.27	0.33	64.65	64.04
HSE	96.00	35.50	60.40	45.70	95.50	22.65	24.87	0.33	66.28	65.86
RPA	101.69	40.50	65.75	50.12	99.79	29.45	27.87	0.32	73.96	71.13

**Table 3. Third-Order Elastic Constants in GPa of CaFI Monolayer**

	$C_{111}$	$C_{112}$	$C_{113}$	$C_{123}$	$C_{133}$	$C_{144}$	$C_{155}$	$C_{166}$	$C_{333}$	$C_{344}$	$C_{366}$	$C_{456}$
LDA	-282	-410	12	-350	-380	-210	-290	-320	-880	-195	-243	310
GGA	-279	-398	20	-347	-371	-198	-274	-310	-860	-178	-239	325
HSE	-260	-395	35	-331	-365	-189	-265	-300	-851	-171	-222	330
RPA	-245	-385	47	-325	-345	-174	-240	-287	-854	-150	-220	348

interaction energies, including improvements in empirical dispersion. It is also worth noting that the RPA correlation energy smoothly incorporates long-range van der Waals interactions. Consequently, RPA is the best way to compute the elastic properties.<sup>61</sup> As previously stated, the elasticity of solids is the material's reaction to applied stresses, which can result in reversible deformations (return to the initial state). Only weak strains are affected by Hooke's law, which states that the strain in a solid elastic is proportionate to the stress. Tensors, often known as stress tensors, are used to express forces. Deformations are the answers, which are also provided by tensors. Because the strain is in the linear phase, the stress/strain ratio (elastic modulus) is constant for tiny stressors. Hooke's law will no longer be met when the strains are that great. So, in the linear realm, in the case of extending, the extension is proportional to the applied force, and in the case of torsion, the angle is proportional to velocity. The theory of elasticity necessitates quantitative expertise to construct a mathematical model of the deformation problem and subsequently to comprehend the formulation and solution techniques. Stress and strain are both described by a 9-element second-rank tensor (see SI). Each portion must be matched with every part for a completely linear relationship between the stress and strain tensors, resulting in a fourth-rank tensor with 81 items. Each member in the entire elasticity tensor  $C_{ijkl} = C_{jikl}$  due to the symmetry of the stress tensor ( $\epsilon_{ij}$ ). Since one of every three parts has an asymmetric companion, the number of single components is instantly 54. Second, because of the symmetry of the strain tensor, each item in the entire elasticity tensor  $C_{ijkl} = C_{ijlk}$ . The number of single items is suddenly 36, a one-third reduction. Since the strain energy involvement of one elastic constant relies on  $C_{ijkl}\epsilon_{ij}\epsilon_{kl}$  altering the form to  $C_{klij}\epsilon_{kl}\epsilon_{ij}$  must not change the overall strain energy, resulting in  $C_{ijkl} = C_{klij}$  there is an extra strain-energy symmetry. The number of separate elements is immediately 21. The 21 parts can then be shown in an asymmetric  $6 \times 6$  s-rank tensor or paradigm, which describes a 6-element first-rank stress tensor or vector to an identical strain vector, using the Voigt notation. The elements of the stress and strain vectors are  $\sigma_{ii} \rightarrow \sigma_i$  and  $\epsilon_{ij} \rightarrow \epsilon_i$  for axial stresses and strains, and  $\sigma_{23} \rightarrow \sigma_4$ ,  $\sigma_{31} \rightarrow \sigma_5$  and  $\sigma_{12} \rightarrow \sigma_6$  for shear stresses, with corresponding, multiplied shear strains  $2\epsilon_{23} \rightarrow \epsilon_4$ ,  $2\epsilon_{31} \rightarrow \epsilon_5$  and  $2\epsilon_{12} \rightarrow \epsilon_6$ . We will refer to all shear stresses as  $\tau_i$  and strains as  $\gamma_i$ . The coefficients then move from 4 subindices to 2 subindices, every changing from 1 to 6. Supposing Hookean linear elasticity, 9 of the 21 elements of the Voigt tensor instantly vanish, particularly, those relating shear stresses to axial strains and axial stresses to shear strains,

leaving 12 elements. The elements thus eliminated are 14, 15, 16, 24, 25, 26, 34, 35, and 36. Three of the remaining 12 relate shear stress in one sense to shear strain in another sense, and thus also vanish under Hookean linear elasticity. The elements thus eliminated are 45, 56, and 46. In the tetragonal system (our case), only 9 elements remain, in three categories: the first one is axial ( $C_{11}$ ,  $C_{22}$ ,  $C_{33}$ ). The second is axial due to the Poisson effect ( $C_{12}$ ,  $C_{13}$ ,  $C_{23}$ ) and the last one is shear ( $C_{44}$ ,  $C_{55}$ , and  $C_{66}$ ). By symmetry of the tetragonal lattice, we can get  $C_{11} = C_{22}$ ,  $C_{13} = C_{23}$ , and  $C_{44} = C_{55}$ . This leaves 6 unique elements, which are the ones you have,  $C_{11}$ ,  $C_{12}$ ,  $C_{13}$ ,  $C_{33}$ ,  $C_{44}$ , and  $C_{66}$ . We present in Table 2 the second-order elastic constants together with Young's modulus, shear modulus, and Poisson's ratio values. Our LDA and GGA SOECs estimations of CaFI have underestimated these constants in comparison with the RPA calculations. For example, the  $C_{11}$  value is around 90.26 and 95.75 GPa with LDA and GGA, respectively. While the HSE functional increases the LDA and GGA calculations, it also underestimates SOECs, as mentioned in Table 2. Here we compare our LDA, GGA, HSE calculations with our RPA results because the RPA approach is the best means to represent the elastic constants.<sup>61</sup> Also, note that in RPA the exact-exchange energy cancels the spurious self-interaction error present in the Hartree energy exactly. Additionally, the RPA correlation energy can be observed as the simplest approximation within the exact formulation of electronic correlation energy in terms of the adiabatic connection and the pairing matrix. As noted in Table 2, the values of SOECs contented the criteria (see SI), which implies that the CaFI 2D monolayer is elastically stable. The  $C_{11}$  elastic constants value is around 101.69 GPa, which explains that this sheet has high incompressibility under uniaxial stress along the crystallographic axis ( $\epsilon_{11}$ ). The SOECs constants are established from total energy estimates of single-crystal physical behavior regularly. In this situation, we have used the values of SOECs to describe mechanical parameters like Young's modulus with DFT and RPA. During our computations, we have determined the Voigt–Reuss–Hill values to identify the precise quantities of the mechanical properties. Table 2 sums the results of the bulk modulus, shear modulus, Young's modulus, and Poisson's ratio. Hitherto, we have detected that the LDA predictions underestimate  $G_{VRH}$  and  $E_{VRH}$  by around  $\sim 6$  and  $\sim 15$  GPa, respectively, in comparison with the RPA computations. Besides, the GGA calculations underestimate  $G_{VRH}$  and  $E_{VRH}$  by about  $\sim 3$  and  $\sim 9$  GPa, respectively. The HSE computations are increasing the LDA and GGA results and they underestimate  $G_{VRH}$  and  $E_{VRH}$

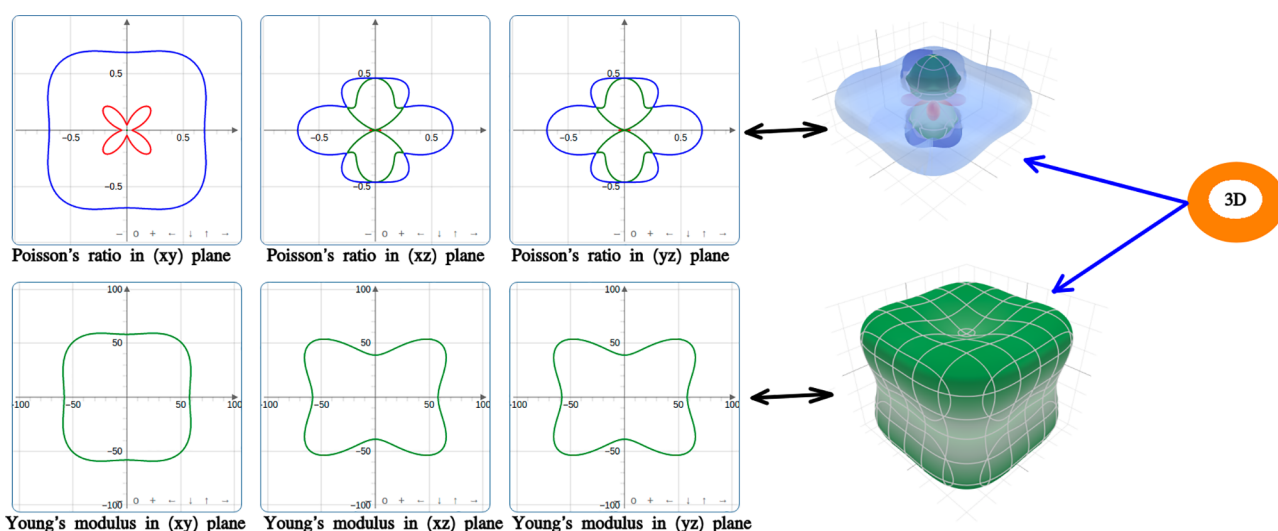


**Figure 10.** Young's modulus and Poisson's ratio of CaFI monolayer are spatially dependent.

by around 2 and 6 GPa always in comparison with the RPA calculations. TOECs estimated of CaFI monolayer are depicted in Table 3, employing DFT and RPA computations. The third-order elastic constants are suitable for determining a variety of thermodynamic conductivities that are related to the anharmonic character of the lattice electric potential. As SOECs, the RPA approach corrects the LDA, GGA, and HSE estimations, for instance, we obtained the  $C_{111}$  and  $C_{112}$  values are approximately  $-245$  and  $-385$  GPa (RPA), respectively. We highly expect the RPA calculations to be very close to the experimental results. We note that there are no experimental or theoretical values for this compound about SOECs and TOECs. In Figure 10, we outline Young's modulus and Poisson's ratio of CaFI monolayer with the RPA predictions in three-dimensional (3D) plot, as well as two-dimensional (2D) projections on the  $(xy)$ ,  $(xz)$ , and  $(yz)$  planes. It also consists of the analysis by presenting the minimum and maximum Young's modulus values, which are approximately  $-60$  and  $60$  GPa, accordingly. Following that, we have employed optical and elastic properties to figure CaFI longitudinal acoustic (LA) phonon dispersion. Because the transverse mode does not appear for  $180^\circ$  backscattering in the experimental study,<sup>62</sup> only the longitudinal acoustic mode was explored. Numerous investigations on the dispersion of the longitudinal acoustic mode propagating along the  $[001]$  crystal axis in semiconductors have been published in the literature. Stoddart et al.,<sup>63</sup> for example, proposed a reasoned method to partially resolve the systematic inaccuracy between surface Brillouin spectroscopy and ultrasonic measurements. Kuok et al.<sup>62</sup> calculated the LA mode velocities of silicon (Si) and germanium (Ge) using Brillouin spectroscopy data and published measurements of their complicated refractive indices. In this regard, we have investigated the wave vector  $q$  of the CaFI monolayer longitudinal acoustic mode. From the computed acoustic phonon dispersion,<sup>62</sup> the wave velocity of the LA phonon propagating in the  $(001)$  direction was resolved at hypersonic frequencies. Here, the optical constants are utilized to calculate sound velocities. Principal, we have calculated the wavelengths  $\lambda$  (nm) from the energies, which are shown in the absorption coefficient spectrum Figure 8. Next, using the medium's complex refractive index values Figure 9, we have computed for each wavelength its wave vector ( $q$ ),

employing the equations, which are presented in SI. In Table 4, we present  $\lambda$  (nm) and the phonon frequencies (THz)

**Table 4.** Wavelengths, Refractive Index ( $\eta$  and  $\kappa$ ), and Observed Frequencies of the Brillouin Peaks in the CaFI Sheet Together with the Corresponding Wave Vectors

CaFI monolayer					
$\lambda$ (nm)	$\eta$	$\kappa$	frequency (THz)	wave vector A ( $10^5 \text{ cm}^{-1}$ )	wave vector H ( $10^5 \text{ cm}^{-1}$ )
174.92	1.72	0.11	3.10	12.37	12.48
207.11	1.61	0.10	2.75	9.78	9.88
276.00	1.54	0.048	2.50	7.00	7.12
354.48	1.44	0.038	2.10	5.00	5.11
414.00	1.43	0.035	2.00	4.34	4.45
496.80	1.41	0.031	1.80	3.56	3.67

together with the phonon wave vectors, using the BSE method. As mentioned for silicon and germanium in refs.,<sup>64,65</sup> we have also computed the phonon wave vectors in two sets (A and H), using  $\eta$  and  $\kappa$  values. Besides, we have studied the LA phonon frequencies against the two sets of phonon wave vectors, as shown in Table 4. The maximum match was obtained for the set H of wave vectors and when the origin is implicated, as shown in Table 5. We have demonstrated that the set H of wave vectors received excellent fits. We have revealed that the corresponding fitted lines have gradients (taking into consideration all mistakes below) of  $1351.20 \pm 4.0$  (A) and  $1346.50 \pm 2.1$  (H)  $\text{Hz/m}^{-1}$ , resulting in values of  $8394 \pm 60$  m/s and  $8387 \pm 10$  m/s for appropriate with and without the origin, respectively, for the velocity of its LA mode propagating

**Table 5.** Results from Linear Fit ( $R$  Is the Agreement Factor with  $R = 1$  Signifying a Ideal Fit),  $\nu$  (GHz) =  $Fq + b$ , to the CaFI Dispersion Curves Obtained from the Data in Table 4

CaFI monolayer			
	slope ( $F$ in GHz cm)	constant ( $b$ in GHz)	$R$
set A	13.51	$-0.090$	0.9999
	$\pm 0.04$	$\pm 0.942$	
set H	13.46	$-0.050$	1
	$\pm 0.021$	$\pm 0.02$	

in the CaFI monolayer. We have noted that the longitudinal acoustic wave velocity value in our sheet is greater than the LA wave velocity experimental value in Ge.<sup>62,66,67</sup> Additionally, the velocity calculated by McSkimin and Andreatch<sup>67</sup> using ultrasonic measurements on n-type 45  $\Omega\text{cm}$  at 20 MHz (Ge) is higher than the velocity predicted by BSE. A noticeable point is that the experience has demonstrated that the wave velocities of the bulk and surface acoustic modes in opaque materials obtained via inelastic light scattering are frequently lower than identical obtained values by ultrasonic techniques. In parallel, the dispersion curves, with wave vectors based for the own LA modes in CaFI, are illustrated in Figure 11. The designer notes that the linear fit, which corresponds to the formation and removal of the origin, matches the graphical scales employed.

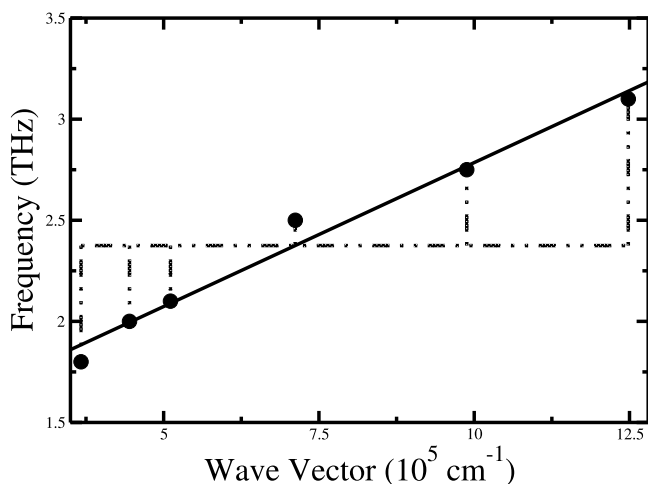


**Figure 11.** Dispersion of the LA mode in the CaFI monolayer. The straight line is the least-squares fit including and without (the points) the origin.

## CONCLUSION

In summary, we have computed the structural, vibrational, electronic, optical, and elastic properties of a new CaFI thin film, using DFT and beyond with GW, RPA, and BSE approaches. The indirect GW band gap energy value of this layer is 6.52 eV, which is greater than the band gap value obtained of PbFCl (6.38 eV with GW), ScOI, and InOF (4.0 eV with HSE) 2D monolayers. Because the spectra begin with a value difference of 0 eV, we established that the absorption coefficient spectrum of the CaFI depicts the semiconductor character of this film. With the BSE methodology, this layer has an excellent absorption coefficient in the 2.50–7.00 eV area. As a result, we have discovered that when the frequency of the incoming light is greater than the photon energy (6.50 eV), the material investigated here becomes translucent. Also, we have obtained  $R$  increases to about 0.107% (6.9 eV), then starts to decrease. SOECs, TOECs, Young's modulus, shear modulus, and Poisson's ratio values are all adequately represented. We also used optical and elastic properties to investigate CaFI LA phonon dispersion. In this context, we have shown that the longitudinal acoustic wave velocity in our sheet is greater than the LA wave velocity of Ge obtained using Brillouin or ultrasonic techniques. Exfoliation, we believe, will provide this material to experimenters. As a consequence, it can be used in the manufacturing of different devices, notably

optical computers. What stands out about this work is that it has a wide gap but still qualifies as a semiconductor. We believe that the CaFI monolayer primarily offers up new possibilities in field-effect transistors, an emerging field that differs from traditional electronics in that it leverages the electron's quantum spin characteristic in addition to its electrical current.

## ASSOCIATED CONTENT

### Supporting Information

The Supporting Information is available free of charge at <https://pubs.acs.org/doi/10.1021/acsomega.1c06437>.

Additional details regarding our calculations and GGA-data of our 2D CaFI structure (PDF)

## AUTHOR INFORMATION

### Corresponding Author

Mohamed Barhoumi – *Laboratoire de la Matière Condensée et des Nanosciences (LMCN), Université de Monastir, Département de Physique, Faculté des Sciences de Monastir, 5019 Monastir, Tunisia;* [orcid.org/0000-0002-3238-5510](https://orcid.org/0000-0002-3238-5510); Email: [med.ferrybn@gmail.com](mailto:med.ferrybn@gmail.com)

### Author

Noureddine Sfina – *College of Sciences and Arts in Mahayel Asir, Department of Physics, King Khalid University, 61421 Abha, Saudi Arabia; Laboratoire de la Matière Condensée et des Nanosciences (LMCN), Université de Monastir, Département de Physique, Faculté des Sciences de Monastir, 5019 Monastir, Tunisia*

Complete contact information is available at:

<https://pubs.acs.org/doi/10.1021/acsomega.1c06437>

### Notes

The authors declare no competing financial interest.

## ACKNOWLEDGMENTS

I want to thank all the researchers who helped me do this time-consuming work, in particular, D. J. Lockwood (Institute for Microstructural Sciences, National Research Council, Ottawa, Ontario, Canada K1A 0R6). In fact, I thank from all the depths of my heart the researchers who belong to the University of Monastir in Tunisia. They have discussed with me the results that you get on this job. Authors are grateful to King Khalid University for their continuous support during conduction of this work.

## REFERENCES

- (1) Castro Neto, A. H.; Guinea, F.; Peres, N. M. R.; Novoselov, K. S.; Geim, A. K. The electronic properties of graphene. *Rev. Mod. Phys.* **2009**, *81*, 109.
- (2) Novoselov, K. S.; Geim, A. K.; Morozov, S. V.; Jiang, D.; Zhang, Y.; Dubonos, S. V.; Grigorieva, I. V.; Firsov, A. A. Electric field effect in atomically thin carbon films. *Science* **2004**, *306*, 666–9.
- (3) Geim, A. K.; Grigorieva, I. V. Van der Waals heterostructures. *Nature* **2013**, *499*, 419–25.
- (4) Li, X. S.; Cai, W. W.; An, J. H.; Kim, S.; Nah, J.; Yang, D. X.; Piner, R.; Velamakanni, A.; Jung, I.; Tutuc, E.; Banerjee, S. K.; Colombo, L.; Ruoff, R. S. Large-Area Synthesis of High-Quality and Uniform Graphene Films on Copper Foils. *Science* **2009**, *324*, 1312.
- (5) Kim, K. S.; Zhao, Y.; Jang, H.; Lee, S. Y.; Kim, J. M.; Kim, K. S.; Ahn, J. H.; Kim, P.; Choi, J. Y.; Hong, B. H. Large-scale pattern

growth of graphene films for stretchable transparent electrodes. *Nature* **2009**, *457*, 706.

(6) Nair, R.; Blake, P.; Grigorenko, A.; Novoselov, K.; Booth, T.; Stauber, T.; Peres, N.; Geim, A. Fine Structure Constant Defines Visual Transparency of Graphene. *Science* **2008**, *320*, 1308.

(7) Morozov, S. V.; Novoselov, K. S.; Katsnelson, M. I.; Schedin, F.; Elias, D. C.; Jaszczak, J. A.; Geim, A. K. Giant intrinsic carrier mobilities in graphene and its bilayer. *Phys. Rev. Lett.* **2008**, *100*, 016602.

(8) Lin, Y. M.; Dimitrakopoulos, C.; Jenkins, K. A.; Farmer, D. B.; Chiu, H.-Y.; Grill, A.; Avouris, P. 100-GHz transistors from wafer-scale epitaxial graphene. *Science* **2010**, *327*, 662.

(9) Gregg, B. A. The Photoconversion mechanism of excitonic solar cells. *MRS Bull.* **2005**, *30*, 20.

(10) Huang, Y.; Sutter, E.; Shi, N. N.; Zheng, J.; Yang, T.; Englund, D.; Gao, H. J.; Sutter, P. Reliable exfoliation of large-area high-quality flakes of graphene and other two-dimensional materials. *ACS Nano* **2015**, *9*, 10612–10620.

(11) Feng, Q.; Mao, N.; Wu, J.; Xu, H.; Wang, C.; Zhang, J.; Xie, L. Growth of  $\text{MoS}_2(1-x)\text{Se}_x$  ( $x = 0.41\text{--}1.00$ ) monolayer alloys with controlled morphology by physical vapor deposition. *ACS Nano* **2015**, *9*, 7450–7455.

(12) Miró, P.; Audiffred, M.; Heine, T. An atlas of two-dimensional materials. *Chem. Soc. Rev.* **2014**, *43*, 6537–6554.

(13) Coleman, J.; Lotya, M.; O'Neill, A.; Bergin, S.; King, P.; Khan, U.; Young, K.; Gaucher, A.; De, S.; Smith, R.; Shvets, I.; Arora, S.; Stanton, G.; Kim, H.; Lee, K.; Kim, G.; Duesberg, G.; Hallam, T.; Boland, J.; Wang, J.; Donegan, J.; Grunlan, J.; Moriarty, G.; Shmeliov, A.; Nicholls, R.; Perkins, J.; Grievson, E.; Theuwissen, K.; McComb, D.; Nellist, P.; Nicolosi, V. Two-Dimensional nanosheets produced by liquid exfoliation of layered materials. *Science* **2011**, *331*, 568–571.

(14) Xia, F.; Wang, H.; Jia, Y. Rediscovering black phosphorus as an anisotropic layered material for optoelectronics and electronics. *Nat. Commun.* **2014**, *5*, 4458.

(15) Koenig, S. P.; Doganov, R. A.; Schmidt, H.; Neto, A. H. C.; Ozyilmaz, B. Electric field effect in ultrathin black phosphorus. *Appl. Phys. Lett.* **2014**, *104*, 103106.

(16) Tao, W.; Lan, J.; Hu, C.; Cheng, Y.; Zhu, J.; Geng, H. Thermoelectric properties of Janus  $\text{MX}_2$  ( $\text{M} = \text{Pd}, \text{Pt}$ ;  $\text{X} = \text{S}, \text{Se}, \text{Te}$ ) transition-metal dichalcogenide monolayers from first principles. *J. Appl. Phys.* **2020**, *127*, 035101.

(17) Burch, K. S.; Mandrus, D.; Park, J. Magnetism in two-dimensional van der Waals materials. *Nature* **2018**, *563*, 47–52.

(18) Gibertini, M.; Koperski, M.; Morpurgo, A. F.; Novoselov, K. S. Magnetic 2D materials and heterostructures. *Nat. Nanotechnol.* **2019**, *14*, 408–419.

(19) Mahmood, A.; Rahman, G. Structural and electronic properties of two-dimensional hydrogenated Xenon. *J. Phys.: Condens. Matter* **2020**, *32*, 205501.

(20) Ma, S.; He, C.; Sun, L. Z.; Lin, H.; Li, Y.; Zhang, K. W. Stability of two-dimensional PN monolayer sheets and their electronic properties. *Phys. Chem. Chem. Phys.* **2015**, *17*, 32009–32015.

(21) Wang, J.; Shu, H.; Zhao, T.; Liang, P.; Wang, N.; Cao, D.; Chen, X. Intriguing electronic and optical properties of two-dimensional Janus transition metal dichalcogenides. *Phys. Chem. Chem. Phys.* **2018**, *20*, 18571–18578.

(22) Guo, S. D.; Wang, Y. H. Thermoelectric properties of orthorhombic group IV–VI monolayers from the first-principles calculations. *J. Appl. Phys.* **2017**, *121*, 034302.

(23) Zhang, W.; Huang, Z.; Zhang, W.; Li, Y. Two-dimensional semiconductors with possible high room temperature mobility. *Nano Res.* **2014**, *7*, 1731.

(24) Hien, N. D.; Nguyen, C. V.; Hieu, N. N.; Kubakaddi, S. S.; Duque, C. A.; Mora-Ramos, M. E.; Dinh, L.; Bich, T. N.; Phuc, H. V. Magneto-optical transport properties of monolayer transition metal dichalcogenides. *Phys. Rev. B* **2020**, *101*, 045424.

(25) Barhoumi, M.; Lazaar, K.; Said, M. DFT study of electronic and optical properties of silicene functionalized with chemical groups. *J. Mol. Graph. Model.* **2019**, *91*, 72–79.

(26) Barhoumi, M.; Abboud, A.; Debbichi, L.; Said, M.; Björkman, T.; Rocca, D.; Lebègue, S. Electronic properties of several two dimensional halides from ab initio calculations. *Beilstein J. Nanotechnol.* **2019**, *10*, 823–832.

(27) Barhoumi, M.; Said, M. Electronic and optical properties of  $\text{PbFCl}$  and  $\text{PbFI}$  monolayers using density functional theory and beyond. *Mater. Chem. Phys.* **2020**, *252*, 123233.

(28) Zheng, C.; Rubel, O.; Kepenekian, M.; Rocquefelte, X.; Katan, C. Electronic properties of Pb-I deficient lead halide perovskites. *J. Chem. Phys.* **2019**, *151*, 234704.

(29) Barhoumi, M.; Said, M. Electronic and optical properties of bismuth oxyhalides from ab initio calculations. *Mater. Sci. Eng., B* **2021**, *264*, 114921.

(30) Hohenberg, P.; Kohn, W. Inhomogeneous Electron Gas. *Phys. Rev.* **1964**, *136*, B864. Kohn, W.; Sham, L. J. Self-Consistent Equations Including Exchange and Correlation Effects. *Phys. Rev.* **1965**, *140*, A1133.

(31) El Haj Hassan, F.; Akbarzadeh, H.; Hashemifar, S. J. Theoretical study of structural and electronic properties of  $\text{CaFI}$ . *J. Phys.: Condens. Matter* **2004**, *16*, 3329.

(32) Guo, Y.; Wang, Q.; Saidi, W. A. Structural stabilities and electronic properties of high-angle grain boundaries in perovskite cesium lead halides. *J. Phys. Chem. C* **2017**, *121*, 1715–1722.

(33) Wang, J.; Deng, M.; Chen, Y.; Liu, X.; Ke, W.; Li, D.; Dai, W.; He, K. Structural, elastic, electronic and optical properties of lithium halides ( $\text{LiF}$ ,  $\text{LiCl}$ ,  $\text{LiBr}$ , and  $\text{LiI}$ ): First-principle calculations. *Mater. Chem. Phys.* **2020**, *244*, 122733.

(34) Tombe, S.; Adam, G.; Heilbrunner, H.; Apaydin, D. H.; Ulbricht, C.; Sariciftci, N. S.; Arendse, C. J.; Iwuoha, E.; Scharber, M. C. Optical and electronic properties of mixed halide ( $\text{X} = \text{I}, \text{Cl}, \text{Br}$ ) methylammonium lead perovskite solar cells. *J. Mater. Chem. C* **2017**, *5*, 1714–1723.

(35) Klejna, S. Structural and electronic properties of multifunctional carbon composites of organometal halide perovskites. *J. Mater. Chem. A* **2019**, *7*, 25020–25031.

(36) Senol, S. D.; Erdem, M. Hydrothermal synthesis of Li co-doped  $\text{Zn}_{0.98}\text{Mg}_{0.02}\text{O}$  nanoparticles and their structural, optical and electrical properties. *Ceram. Int.* **2016**, *42*, 10929–10934.

(37) Löber, M.; Geibenhöner, C.; Ströbele, M.; Romao, C.; Meyer, H. Synthesis, Structure and Electronic Properties of Three Tin Oxide Halides. *Eur. J. Inorg. Chem.* **2021**, *2021*, 283–288.

(38) Giordano, F.; Abate, A.; Correa Baena, J. P.; Saliba, M.; Matsui, T.; Im, S. H.; Zakeeruddin, S. M.; Nazeeruddin, M. K.; Hagfeldt, A.; Graetzel, M. Enhanced electronic properties in mesoporous  $\text{TiO}_2$  via lithium doping for high-efficiency perovskite solar cells. *Nat. Commun.* **2016**, *7*, 10379.

(39) Kresse, G.; Joubert, D. From ultrasoft pseudopotentials to the projector augmented-wave method. *Phys. Rev. B* **1999**, *59*, 1758.

(40) Kresse, G.; Hafner, J. Ab initio molecular dynamics for liquid metals. *Phys. Rev. B* **1993**, *47*, 558.

(41) Ceperley, D. M.; Alder, B. J. Ground state of the electron gas by a stochastic method. *Phys. Rev. Lett.* **1980**, *45*, 566–9.

(42) Perdew, J. P.; Burke, K.; Ernzerhof, M. Generalized Gradient Approximation Made Simple. *Phys. Rev. Lett.* **1996**, *77*, 3865.

(43) Heyd, J.; Scuseria, G. E.; Ernzerhof, M. Hybrid functionals based on a screened Coulomb potential. *J. Chem. Phys.* **2003**, *118*, 8207.

(44) Miyake, T.; Aryasetiawan, F.; Kotani, T.; Van Schilfgaarde, M.; Usuda, M.; Terakura, K. Total energy of solids: An exchange and random phase approximation correlation study. *Phys. Rev. B* **2002**, *66*, 245103.

(45) Dubecky, M.; Karlicky, F.; Minarik, S.; Mitas, L. Fundamental gap of fluorographene by many-body GW and fixed-node diffusion Monte Carlo methods. *J. Chem. Phys.* **2020**, *153*, 184706.

(46) Onida, G.; Reining, L.; Rubio, A. Electronic excitations: density-functional versus many-body Green's-function approaches. *Rev. Mod. Phys.* **2002**, *74*, 601–659.

- (47) Gonze, X.; Lee, C. Dynamical matrices, Born effective charges, dielectric permittivity tensors, and interatomic force constants from density-functional perturbation theory. *Phys. Rev. B* **1997**, *55*, 10355.
- (48) Paier, J.; Marsman, M.; Hummer, K.; Kresse, G.; Gerber, I. C.; Ángyán, J. G. Screened hybrid density functionals applied to solids. *J. Chem. Phys.* **2006**, *124*, 154709.
- (49) Onida, G.; Reining, L.; Rubio, A. *Rev. Mod. Phys.* **2002**, *74*, 601.
- (50) Zolyomi, V.; Drummond, N. D.; Fal'ko, V. I. Electrons and phonons in single layers of hexagonal indium chalcogenides from ab initio calculations. *Phys. Rev. B* **2014**, *89*, 205416.
- (51) Zolyomi, V.; Drummond, N. D.; Fal'ko, V. I. Band structure and optical transitions in atomic layers of hexagonal gallium chalcogenides. *Phys. Rev. B* **2013**, *87*, 195403.
- (52) Tran, F.; Blaha, P. Accurate band gaps of semiconductors and insulators with a semilocal exchange-correlation potential. *Phys. Rev. Lett.* **2009**, *102*, 226401.
- (53) Reining, L. The GW approximation: content, successes and limitations. *WIREs Comput. Mol. Sci.* **2018**, *8*, 1344.
- (54) Ulpe, A. C.; Bredow, T. GW-BSE calculations of electronic band gap and optical spectrum of ZnFe<sub>2</sub>O<sub>4</sub>: Effect of cation distribution and spin configuration. *ChemPhysChem* **2020**, *21*, 546–551.
- (55) Bengtsson, L. Dipole correction for surface supercell calculations. *Phys. Rev. B* **1999**, *59*, 12301.
- (56) Vu, T. V.; Nguyen, C. V.; Phuc, H. V.; Lavrentyev, A. A.; Khyzhun, O. Y.; Hieu, N. V.; Obeid, M. M.; Rai, D. P.; Tong, H. D.; Hieu, N. N. Theoretical prediction of electronic, transport, optical, and thermoelectric properties of Janus monolayers In<sub>2</sub>XO (X = S, Se, Te). *Phys. Rev. B* **2021**, *103*, 085422.
- (57) Tang, K.; Qin, R.; Zhou, J.; Qu, H.; Zheng, J.; Fei, R.; Li, H.; Zheng, Q.; Gao, Z.; Lu, J. Electric-field-induced energy gap in few-layer graphene. *J. Phys. Chem. C* **2011**, *115*, 9458.
- (58) Zheng, F.; Liu, Z.; Wu, J.; Duan, W.; Gu, B. L. Scaling law of the giant Stark effect in boron nitride nanoribbons and nanotubes. *Phys. Rev. B* **2008**, *78*, 085423.
- (59) Liu, Q.; Li, L.; Li, Y.; Gao, Z.; Chen, Z.; Lu, J. Tuning Electronic Structure of Bilayer MoS<sub>2</sub> by Vertical Electric Field: A First-Principles Investigation. *J. Phys. Chem. C* **2012**, *116*, 21556.
- (60) Mak, K. F.; Lui, C. H.; Shan, J.; Heinz, T. F. Observation of an electric-field-induced band gap in bilayer graphene by infrared spectroscopy. *Phys. Rev. Lett.* **2009**, *102*, 256405.
- (61) Barhoumi, M.; Rocca, D.; Said, M.; Lebegue, S. Elastic and mechanical properties of cubic diamond and silicon using density functional theory and the random phase approximation. *Solid State Commun.* **2021**, *324*, 114136.
- (62) Kuok, M. H.; Ng, S. C.; Rang, Z. L.; Lockwood, D. J. Acoustic phonon dispersion at hypersonic frequencies in Si and Ge. *Phys. Rev. B* **2000**, *62*, 12902.
- (63) Stoddart, P. R.; Crowhurst, J. C.; Every, A. G.; Comins, J. D. Measurement precision in surface Brillouin scattering. *J. Opt. Soc. Am. B* **1998**, *15*, 2481.
- (64) Humlicek, J.; Garriga, M.; Alonso, M. I.; Cardona, M. Optical spectra of Si<sub>x</sub>Ge<sub>1-x</sub> alloys. *J. Appl. Phys.* **1989**, *65*, 2827.
- (65) Sandercock, J. R. Brillouin-scattering measurements on silicon and germanium. *Phys. Rev. Lett.* **1972**, *28*, 237.
- (66) McSkimin, H. J.; Andreatch, P., Jr. Elastic Moduli of Silicon vs Hydrostatic Pressure at 25.0° and -195.8°. *J. Appl. Phys.* **1964**, *35*, 2161.
- (67) McSkimin, H. J.; Andreatch, P., Jr. Elastic moduli of germanium versus hydrostatic pressure at 25.0° and -195.8°. *J. Appl. Phys.* **1963**, *34*, 651.